Use of the channeling technique and calculated angular distributions to locate Br implanted into Fe single crystals*

R. B. Alexander†
Clarendon Laboratory, University of Oxford, Oxford, England
and Nuclear Physics Division, Atomic Energy Research Establishment, Harwell, England

P. T. Callaghan
Clarendon Laboratory, University of Oxford, Oxford, England

J. M. Poate
Bell Laboratories, Murray Hill, New Jersey 07974

(Received 5 July 1973)

The channeling and backscattering of ^{4}He and ^{14}N ions of several MeV have been used in an experiment to determine the lattice location of Br implanted into Fe single crystals. Use has been made of fast electronics to reduce pulse pileup in the backscattered energy spectra. Angular scans have been carried out across the three major crystal axes and the three major planes. For the {211} plane a triple peak is observed in the Br-yield curve. This triple peak and a peak observed in the {100} planar scan indicate that a substantial fraction of the Br atoms occupies an interstitial site of low symmetry in the Fe lattice. A systematic analysis reveals three possible interstitial sites qualitatively consistent with the data. Theoretical calculations of angular-yield curves, using both Monte Carlo computer simulations and an analytical model based on the continuum theory of channeling, have been performed. Various possible distributions of Br atoms are considered, and with the aid of the calculated curves a quantitative interpretation of the location is made. Good agreement with the data is obtained for a distribution of 60% of the Br in one of the interstitial sites and the remaining 40% substitutional. Possible physical interpretations of this result, and its significance for hyperfine field measurements on Br implanted in Fe, are briefly discussed.

I. INTRODUCTION

One of the most useful applications of ion channeling has been the location of foreign atoms (usually implanted) in crystal lattices. When the foreign atoms are substitutional, the interaction yield (for example, from backscattering) for a channeled beam is attenuated in the same way for both foreign and lattice atoms.[1] In the case of interstitial foreign atoms, close to the center of a particular channel, a peak or multiple peak is observed in the angular-yield curve due to the flux-peaking effect for channeled ions.[2-5] The existence of flux peaking makes it essential to carry out complete angular scans across the major crystal channeling directions in order to resolve the location of impurity atoms in a crystal.

Angular scans about channeling directions have been used to determine the lattice location of interstitial atoms in a number of recent experiments. Flux-peaking effects have been observed for interstitial impurities in Si[3,6,7] and in W and Fe.[8,9] Angular scans can also be used to locate atoms in interstitial sites only slightly displaced from lattice sites. In this case the interaction yield shows a dip, but it is narrower than that obtained when the atoms are substitutional. Such an effect has been employed[10] to distinguish between Bi atoms in lattice sites and in positions displaced 0.45 Å from lattice sites in Si.

In this paper an extensive experiment on the lattice location of ^{81}Br implanted into Fe single crystals is described. Backscattering of ^{4}He and ^{14}N ions of several MeV was used. The work was initiated in order to elucidate the results of hyperfine-interaction measurements on Br implanted in Fe.[11] The experiment has also shown several interesting features which indicate some of the ultimate possibilities and limitations of the location technique itself. Because of the small mass resolution between Br and Fe in the backscattered energy spectrum, the background under the Br peak due to electronic pulse pileup can be large. Methods of minimizing the effect of this background are discussed. Angular scans across the three major crystal axes and the three major planes in Fe have been carried out. For the {211} plane a triple peak is observed in the Br-yield curve, the first time such a feature has been seen experimentally. This triple peak, and a peak observed in the {100} planar scan, indicate that a substantial fraction of the Br atoms must occupy an interstitial site of low symmetry in the Fe lattice.

Theoretical calculations of angular-yield curves have been employed to make a quantitative interpretation of the results. The calculations have been performed using both Monte Carlo computer simulations[2,11] (binary-collision model) and an analyti-

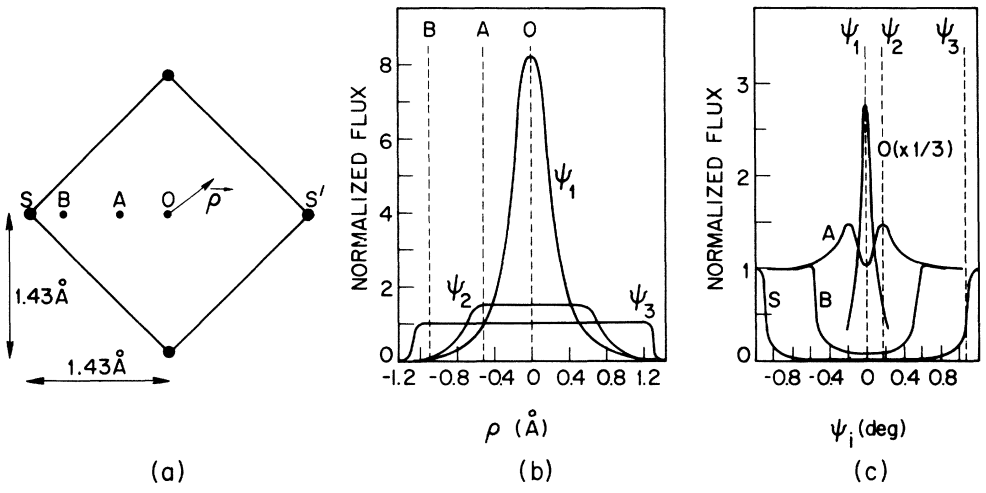

FIG. 1. Illustrating the use of the flux-peaking effect for channeled ions in distinguishing between atoms in different positions in a channel. (a) Cross section of a ⟨100⟩ axial channel in the bcc Fe lattice, showing four distinct sites—O, A, B, and S. The filled circles represent rows of Fe atoms. (b) Spatial flux distributions along the line SOS' in (a), for 3.5-MeV ^{14}N ions incident at three different angles to the channel axis; $\psi_1 = 0$ and ψ_3 is the critical angle for channeling ($\psi_1 < \psi_2 < \psi_3$). The distributions were calculated using the analytical model described in Appendix B, and the flux is normalized to the random value. (c) Calculated fluxes at the sites O, A, B, and S, respectively, in (a), as a function of the angle of incidence ψ_i. For each site a distinctive angular behavior is seen.

cal model based on the continuum theory of channeling.[12] Several possible physical models for the Br location are discussed. Finally, the implications of the location results for nuclear orientation measurements of the hyperfine field at Br in Fe are briefly considered. A preliminary report on the work has been presented elsewhere.[13]

II. INTERPRETATION OF CHANNELING EXPERIMENTS FOR ATOM LOCATION

Owing to the existence of flux peaking, the interaction yield for a well-channeled beam (χ_0) may correspond to several different distributions of foreign atoms, and the consequent need for carrying out complete angular scans complicates the experiments. However, the flux-peaking effect is useful in the interpretation of these experiments, as the narrow angular width of the effect (compared to the critical angle for channeling) makes it sensitive to the exact position of interstitial atoms.

The ability of the technique to distinguish between atoms in different positions in a channel can be seen from Fig. 1. For atoms at the center of the channel, a narrow peak will be observed in the angular yield curve. On the other hand, for atoms displaced from the channel axis, a double peak may be seen. The occurrence of such a double peak has been predicted by several authors.[1,5,14] The effect can be simply understood by considering the transverse energy $E_\perp$ of the channeled ions at the crystal surface:

$$E_\perp = E\psi_i^2 + U(\vec{\rho}_i), \tag{1}$$

where E is the ion energy, ψ_i is the angle of incidence relative to the channel symmetry axis, and $U(\vec{\rho}_i)$ is the transverse channel potential at $\vec{\rho} = \vec{\rho}_i$ ($\vec{\rho}$ is the position vector relative to the channel axis). At some position $\vec{\rho}_d$ displaced from the channel axis, the maximum flux is not attained until the initial transverse energy of those particles entering the channel near the minimum $U(\vec{\rho}_0)$ becomes equal to $U(\vec{\rho}_d)$; that is,

$$E\psi_i^2 = U(\vec{\rho}_d) - U(\vec{\rho}_0). \tag{2}$$

(When multiple scattering is significant the term $E\psi_i^2$ must be replaced by $E\psi_i^2 + \delta E_\perp$, where $\delta E_\perp$ is the increase in $E_\perp$ associated with the multiple scattering.) It is seen from Fig. 1 that a double peak will be observed unless $\vec{\rho}_d$ is sufficiently large that a dip occurs in the yield at $\psi_i = 0$. In this case the magnitude of $\vec{\rho}_d$ can be calculated from the width of the dip. Any combination of these features is possible, depending on the distribution of foreign atoms across the particular channel.

In the location of interstitial atoms, scans across crystal planes can often be more useful than scans across axes. It may be possible to confirm or eliminate a particular interstitial site by a single planar scan. For interstitial sites of low symmetry, more structure will, in general, be observed in planar than in axial scans, since low-symmetry sites are more likely to lie near the center of planar channels than the center of axial channels.

Qualitative information about the location is obtained from (i) the angular position (and, to a lesser extent, the magnitude) of any peaks in the impurity-yield curves, and (ii) the width and magnitude of any dips in the impurity yield, compared with the host-yield dip for the same channeling direction. When all atoms are in substitutional sites or in a simple interstitial site the location will be obvious. However, for more complicated cases the site or sites occupied by the impurity atoms must be deduced using Eq. (2) and by calculating angular-yield curves. Two models that can be used for such calculations are described in Sec. VI B.

III. EXPERIMENTAL DETAILS

A. Choice of analyzing beam

A problem in this type of experiment is that the impurity peak in the backscattered energy spectrum is superimposed on a background. This background arises largely from electronic pulse pileup in the amplifier system. As the pileup intensity is highest near the edge of the host spectrum (see Figs. 5–7), it is important to maximize the relative energy separation between the impurity peak and the host spectrum. For ^{81}Br in Fe (atomic weight 56) this is important because of the small mass difference between the two elements.

The energy separation depends primarily on the kinematics of the elastic scattering process and, to a lesser extent, on the stopping power for the incident ions. For an impurity at the crystal surface, the ratio of the energies of ions backscattered from the impurity and the host is given by the ratio of the respective kinematic factors k_S.[15] This ratio increases with the mass M_1 and thus the atomic number Z_1 of the incident ions. In the case of impurity atoms below the crystal surface, the energy ratio is less (see Fig. 2) owing to the energy lost by the incident particles along the incoming and outgoing trajectories.[15] Although the stopping power ($-dE/dx$) increases more rapidly with Z_1 than the k_S ratio, the energy-loss term is usually small as the impurity atoms are close to the crystal surface. Furthermore, at MeV energies the stopping power for a particular ion either decreases with the ion energy E_0 or increases at most as $E_0^{1/2}$. Hence the relative energy separation between the impurity and the host improves with increasing Z_1 and with increasing energy.

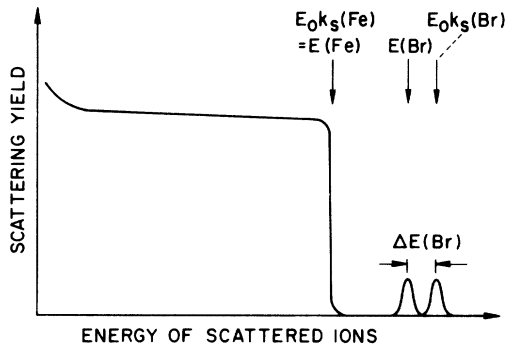

FIG. 2. Schematic backscattered energy spectrum for ions of energy E_0 incident on a Fe target implanted with Br. The energies E(Fe) and E(Br) correspond to scattering from surface Fe atoms and implanted Br atoms, respectively. k_s is the kinematic factor, and ΔE takes into account the energy lost by the incident ions along the incoming and outgoing trajectories.

Apart from good energy separation, several other factors must be taken into account in selecting the analyzing beam. These include beam-induced radiation damage, which must not be significant, and the magnitude of the impurity yield, which varies as $(Z_1/E)^2$.

For most implants in Fe, ^{14}N ions of several MeV appear an optimum choice. Table I compares the energy separation obtainable for ^{81}Br in Fe with 3.0-MeV ^{4}He$^+$ and 3.0-MeV ^{14}N$^+$ ions, respectively. It is seen that the relative separation between the Br peak and the Fe edge is greater for ^{14}N than for ^{4}He, even though the stopping power is considerably larger. Consequently the pileup background under the Br peak is less. (The use of ^{12}C ions to reduce the effect of pileup in backscattering experiments has recently been investigated by Abel *et al.*[18]) The detector resolution is worse for ^{14}N, but this is a less important consideration than pileup effects. In the majority of these experiments 3.5-MeV ^{14}N was used. In those experiments carried out with ^{4}He ions, a system of fast electronics was used to reduce the pileup (Sec. III D).

B. Crystal preparation

The Fe single crystals used in these experiments were obtained (from Metals Research Ltd., England) in the form of cylindrical rods. These had been grown by strain annealing, the purity of the Fe being 99.8%. After orientation by x-ray diffraction each rod was cut into thin disks, approximately 7 mm in diameter and 1 mm thick, perpendicular to a ⟨110⟩ axis (within 2°); a crystal cut perpendicular to a ⟨100⟩ axis was used in some experiments. The crystals were spark planed and then electropolished[11,19] in an electrolyte containing 50-ml perchloric acid and 1000-ml glacial acetic acid. Backscattering measurements indicated a surface oxide layer (stoichiometry Fe_2O_3) on the crystals 30–40 Å in thickness.

Implantation of the stable isotope ^{81}Br was carried out at 80 keV at room temperature. The implants were done on either the Harwell Mk. I electromagnetic separator, using doubly charged ions at 40 kV, or the 300-kV accelerator at Bell Laboratories, us-

TABLE I. Comparison of the calculated energy separation between the Br peak and the Fe edge (see Fig. 2) for $^4He^+$ and $^{14}N^+$ ions of 3.0-MeV incident normal to the surface of the Fe. The scattering angle has been taken as 160°, and the depth of the Br atoms from the crystal surface is assumed to be 300 Å. Values of the detector resolution (for a Si surface-barrier detector) were determined experimentally.

Ion	E(Fe) (MeV)	k_s(Br)/k_s(Fe)	Stopping power in Fe (MeV/μm)	E(Br)/E(Fe)	Detector resolution (keV)
3.0-MeV ^{4}He	2.27	1.09	0.50[a]	1.07	~20
3.0-MeV ^{14}N	1.11	1.36	3.0[b]	1.25	~70

[a]Reference 16. [b]Reference 17.

ing singly charged ions at 80 kV. To minimize channeling effects during implantation, the crystals were tilted ~7° away from the surface normal. For most implants the dose was 5×10^{14} ions/cm^2. The projected range of the ions was 270 Å with a standard deviation of 70 Å (Sec. IV) giving, for the above dose, an average local concentration of 0.35-at.% Br in the implanted region.

C. Experimental arrangement

Two accelerators were employed for the backscattering experiments—the 5-MV Van de Graaff at Harwell and the 2-MV Van de Graaff at Bell Laboratories. All the ^{14}N measurements were done on the Harwell machine. As a ^{14}N beam can be contaminated by molecular impurities, the quality of the beam at the target was checked regularly. This was done by examining the energy spectrum obtained using either backscattering from a thin (~150 Å) Au foil or forward scattering from a thin C foil.

Similar experimental arrangements were used in both laboratories. The incident beam was collimated to a diameter of 1 mm and an angular divergence of less than ±0.03°. Crystal alignment was carried out (with ^{4}He ions) using a goniometer which enables the target to be rotated in steps of 0.01° by means of stepping motors; the Harwell goniometer[20] has three independent axes, the Bell goniometer two axes. Backscattered particles were detected with Si surface-barrier detectors. Two 100-mm^2 detectors {energy resolution [full width at half-maximum (FWHM)] ≈ 20 keV for ^{4}He}, mounted at scattering angles in the range 160° – 170°, were used in the Harwell system (Fig. 3); a 50-mm^2 annular detector (energy resolution ≈ 15 keV) for the experiments at Bell Laboratories. Detector acceptance angles were ≳ 6°, and care was taken to avoid blocking effects for the scattered particles.

The ion dose was measured by integration of the target current, with suitable secondary electron suppression. The target chamber was maintained at a pressure ≲ 10^{-6} Torr, and the target was surrounded by a shield cooled with liquid nitrogen to minimize surface contamination. Further details of the two experimental systems are given elsewhere.[11,21]

D. Pulse pileup rejection

In the measurements performed on the Bell Laboratories 2-MV machine, only ^{4}He ions were used where the background under the Br peak due to pulse pileup is a serious problem (cf. Sec. III A). One method of minimizing the effect is to use low beam currents, since pileup is proportional to the square of the count rate. (Thus the effect is less severe when the incident beam is channeled.) However, for implantation doses ~10^{14} ions/cm^2, reduction of the beam current to a level where the background under the Br peak is negligible would require using excessive amounts of accelerator time. Instead, a system of fast electronics especially designed to minimize pulse pileup[22] was employed (Fig. 4). The preamplifier provides a fast

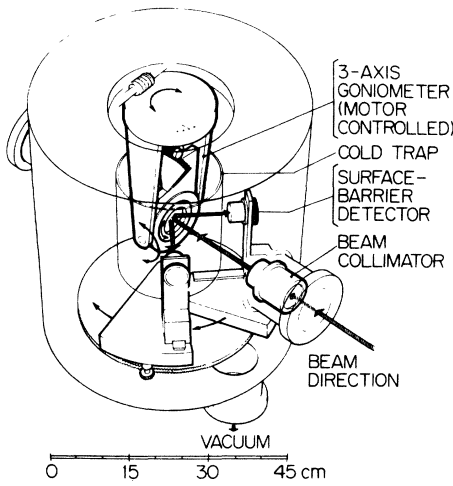

FIG. 3. Schematic representation of the target chamber and three-axis goniometer used in the experiments carried out with the Harwell 5-MV Van de Graaff accelerator.

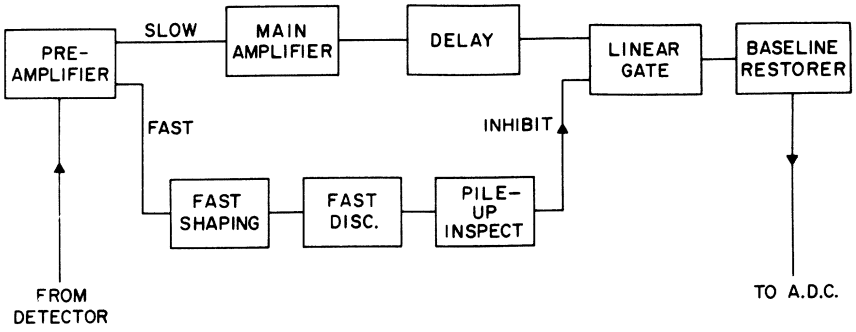

FIG. 4. Block diagram of the electronics used for pulse pileup rejection. The preamplifier provides both a slow and a fast output signal. Information derived from the fast-signal line is used to reject pileup pulses in the slow-signal line.

output signal which is fed into a fast wide-band amplifier (rise time ~5 nsec). This amplifier is capable of resolving the pulses that give rise to pileup in the slower main amplifier: the pileup inspector is used to reject such pulses.

Figure 5 shows typical results obtained with this system. It is seen that the background under the Br peak is reduced considerably, while there is a negligible loss of counts from the Fe spectrum.

IV. EXPERIMENTAL RESULTS

Typical backscattered energy spectra are shown in Figs. 6 and 7, for ^{4}He and ^{14}N ions, respectively with the energy windows over which the Br and Fe yields were summed. It was necessary to correct the counts in the Br window for background, which was typically no more than about 20% of the total counts. As the background was generally not linear, a background fit was drawn by hand; all experimental errors include the uncertainty involved in this method of correction.

The Fe window was set to correspond to scattering from Fe atoms at the same depth from the crystal surface as the Br atoms. This depth was determined experimentally by measuring the difference in energy between ^{14}N ions backscattered from the implanted Br and ions backscattered from surface Br in a KBr crystal. The energy difference is related to the projected range and the random stopping power. The result obtained for the mean projected Br range $\bar{R}_p$ was 270 ± 40 Å, with an associated standard deviation $\Delta\bar{R}_p$ (calculated from the width of the implanted Br peak) of 70 ± 20 Å. The channeled stopping power was assumed to be equal to the random stopping power, so that the energy window remained fixed throughout. Values of the stopping power for ^{4}He ions in Fe were taken from Ref. 16, those for ^{14}N ions from Ref. 17 (though recent experimental work[23] suggests that the actual values for ^{14}N may be slightly higher).

Several different impurity peaks were occasionally observed in the aligned spectra. These were

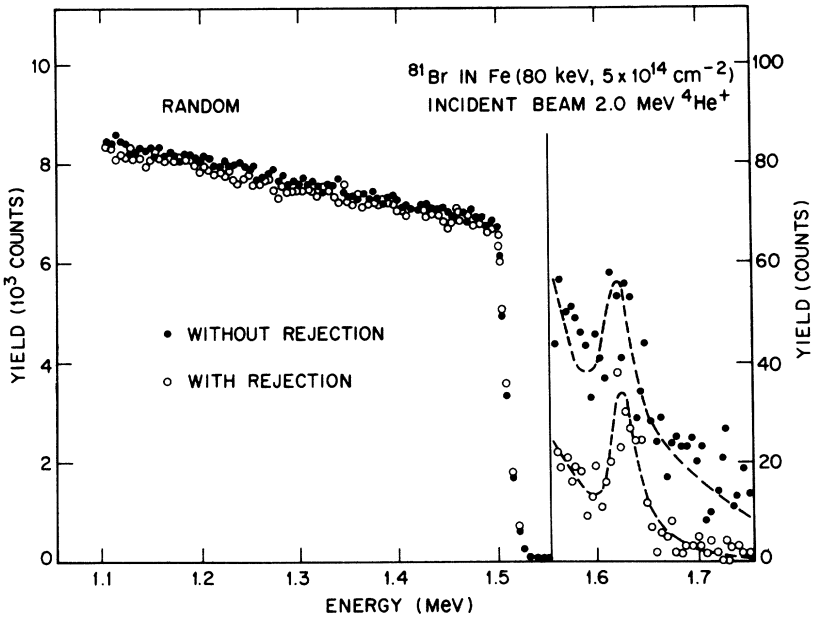

FIG. 5. Backscattered energy spectra for 2.0-MeV ^{4}He$^+$ ions incident in a random direction in a Fe single crystal implanted with Br, showing the effect of using the pileup rejection system in Fig. 4. The vertical scale has been expanded in the vicinity of the Br peak. Both the beam current and total integrated current were the same for the two spectra.

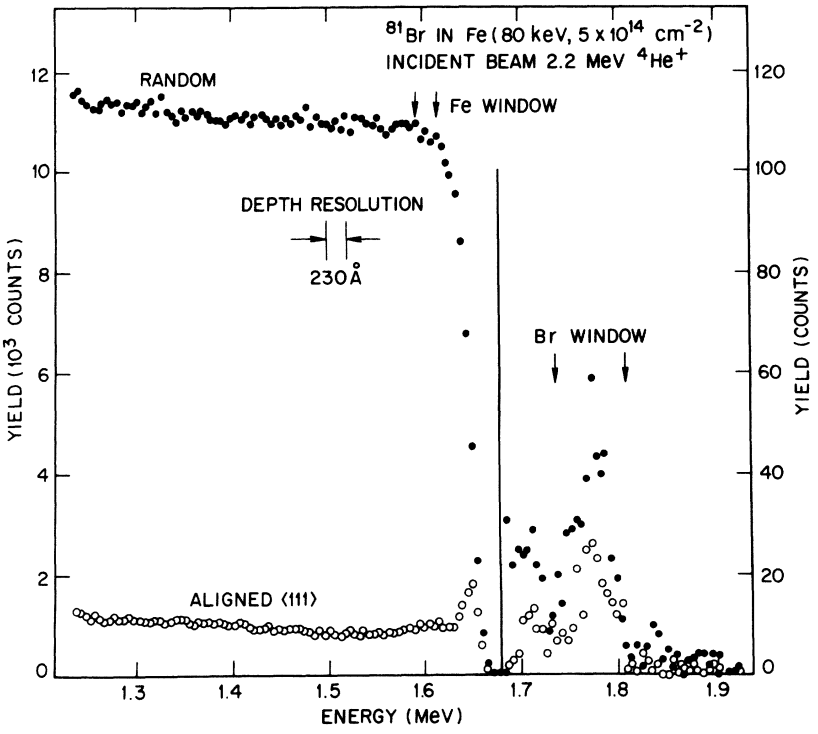

FIG. 6. Backscattered energy spectra for 2.2-MeV $^{4}He^{+}$ ions incident in ⟨111⟩ and random directions in a Fe single crystal implanted with Br. In the high-energy region the vertical scale has been expanded. The integrated target current was the same in both cases.

identified from the scattering kinematics as Mn, Cu and Hg or Pb, probably deposited on the crystal surface from the electropolishing solution (Sec. III B). In Fig. 6 a small peak due to Cu can be seen at 1.71 MeV; the area under the peak corresponds to an average thickness of $\sim 10^{-2}$ of a monolayer. It was verified, using an unimplanted Fe crystal, that there were no surface impurity peaks in the region corresponding to the Br peak.

Table II summarizes the results of all Br and Fe χ_0 measurements, where χ_0 is the ratio of the aligned to random yield, for various implantation doses, analyzing beams, and crystal directions. Random spectra were taken in carefully chosen orientations and corrected where necessary for thickness effects. Where data have been taken from an angular scan this is indicated. For channels where more than one measurement was made, good agreement is obtained between the different results.

Although most experiments were performed on crystals implanted at 5×10^{14} ions/cm^2, some measurements were also performed on crystals implanted at lower and higher doses. The implantation doses were checked by measuring the Br yield for a beam incident in a random direction. In all cases, the dose determined in this way agreed with the dose measured in the implantation to within a factor of 1.5.

As the χ_0 results indicated that a substantial fraction of the Br was not substitutional, angular scans were carried out across the three major crystal axes and the three major planes. For all scans the Br dose was 5×10^{14} ions/cm^2, and most of the scans were done with ^{14}N. This was partly because of the background problem discussed previously, and partly because the critical angles for channeling are larger for ^{14}N than ^{4}He (at the same energy), resulting in a greater angular resolution for the same beam divergence. Figures 8 and 9

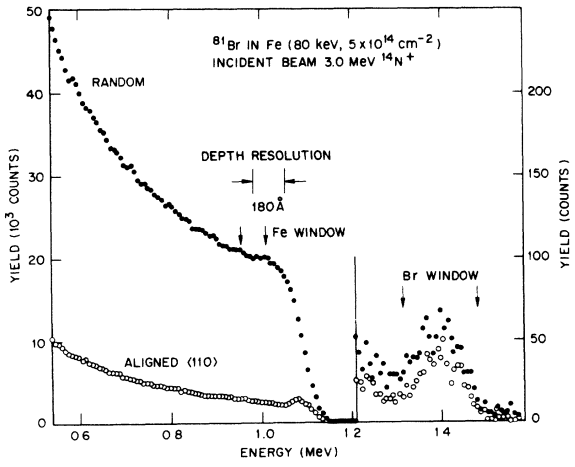

FIG. 7. As in Fig. 6, for 3.0-Mev $^{14}N^{+}$ ions incident in ⟨110⟩ and random directions.

TABLE II. χ_0 measurements for Br implanted into Fe single crystals, including values taken from angular scans. Errors in χ_0(Fe) are $\lesssim 5\%$.

Br dose (ions/cm^2)	Channel	Analyzing beam	Energy (MeV)	χ_0 or complete scan	χ_0(Br)	χ_0(Fe)
5×10^{14}	⟨111⟩	He	2.2	Scan	0.56 ± 0.04	0.075
			4.0	χ_0	0.52 ± 0.05	0.071
		N	3.0	χ_0	0.51 ± 0.04	0.081
	⟨100⟩	He	2.2	Scan	0.59 ± 0.06	0.070
			4.0	χ_0	0.64 ± 0.12	0.12
		N	3.0	Scan	0.56 ± 0.10	0.12
			3.5	Scan	0.58 ± 0.06	0.075
	⟨110⟩	He	2.2	χ_0	0.69 ± 0.08	0.10
			4.0	χ_0	0.80 ± 0.11	0.12
		N	3.0	Scan	0.62 ± 0.04	0.13
	{110}	He	1.8	χ_0	0.67 ± 0.06	0.43
			2.2	Scan	0.59 ± 0.06	0.37
		N	3.5	χ_0	0.66 ± 0.06	0.31
			3.5	Scan	0.67 ± 0.05	0.365
	{100}	He	2.2	Scan	0.93 ± 0.07	0.55
		N	3.5	χ_0	1.00 ± 0.05	0.545
			3.5	Scan	0.99 ± 0.04	0.55
	{211}	N	3.5	Scan	0.87 ± 0.04	0.635
			3.5	Scan[a] (i)	0.81 ± 0.05	0.75
				(ii)	1.14 ± 0.06	0.78
	{111}	N	3.5	χ_0	0.85 ± 0.10	0.86
1×10^{14}	⟨111⟩	N	3.5	χ_0	0.53 ± 0.10	0.059
	⟨100⟩	N	3.5	χ_0	0.60 ± 0.10	0.083
	⟨110⟩	N	3.5	χ_0	0.80 ± 0.10	0.080
2×10^{15}	⟨100⟩	He	2.0	χ_0	0.64 ± 0.05	0.088
	⟨110⟩	He	2.0	χ_0	0.81 ± 0.05	0.14
	{110}	He	2.0	χ_0	0.85 ± 0.06	0.40
5×10^{15}	⟨111⟩	He	4.0	χ_0	0.56 ± 0.05	0.17
5×10^{14}	⟨111⟩	N	3.5	Scan	1.02 ± 0.08	0.037
(annealed)[b]	⟨100⟩	N	3.5	χ_0	1.00 ± 0.08	0.033
Unimplanted crystal	⟨111⟩	N	3.0	χ_0		0.028

[a]Scans (i) and (ii) showing effect of apparent enhanced diffusion of N in Fe (Sec. V B).
[b]Annealed for 30 min at 600 °C.

show the results of the scans; the tilting planes in which the scans were carried out are given in Table III. The ratio of the critical angles for the three axes, and that for the three planes, are in reasonable agreement with channeling theory.[12] The Br yield (excluding background) varied between 300 and 1200 counts per point. Typical currents were 1 nA for the ^{14}N measurements and 3 nA for ^{4}He, and typical doses for each angular position were 5 μC for ^{14}N and 10 μC for ^{4}He on ~1-mm^2 beam spots.

For the ⟨100⟩ axis and {110} plane, scans were performed with both ^{14}N and ^{4}He, and it is seen that the results are essentially the same. The shoulder in the Br curve in the ⟨100⟩ ^{4}He scan does not appear in the ^{14}N scan, but this can be attributed to the different tilting planes in the two cases (see Table III). In the {110} scans, the points of inflection in the Br dip for ^{14}N are not resolved in the ^{4}He curve. A ^{4}He scan (not shown) was also performed for the {100} plane, showing good agreement with the ^{14}N data.

The yield curves for all three axes are rather featureless. In each case there is a dip in the Br yield, of approximately half the width and half the magnitude of the Fe dip; the Br dip in the ⟨110⟩ scan is slightly weaker than for the other two axes.

However, in the planar scans (Fig. 9) some definite structure is observed. For the {100} plane a flux peak is seen in the Br yield, the peak being superimposed on a dip. In the {211} scan there is a *triple peak*, which consists of a single central peak together with a double peak, superimposed on a dip. That the triple-peak structure exists can be seen more clearly if the scan is folded over about the center, as shown in Fig. 10. The measured position of the double peak is $\psi_t = 0.16° \pm 0.03°$ [cf. $\psi_{1/2}$(Fe) = 0.42°].

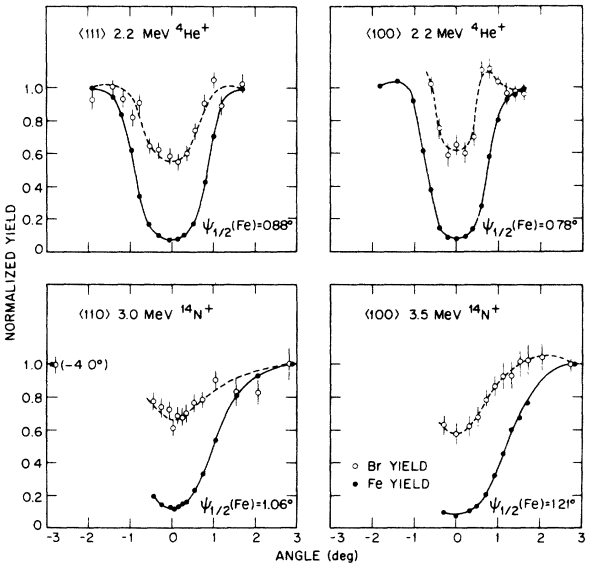

FIG. 8. Angular scans across ⟨111⟩, ⟨100⟩, and ⟨110⟩ axes in Br-implanted Fe single crystals, with the type and energy of ion used for each scan indicated. The Br and Fe yields have been normalized to the random values. The smooth curves drawn through the Br and Fe points are only to guide the eye. Shown in each case is the experimental critical angle for channeling $\psi_{1/2}$(Fe).

V. RADIATION DAMAGE AND BEAM EFFECTS

A. Radiation damage

The implantation of Br introduces disorder into the Fe crystals. A measure of the damage produced is given by the aligned backscattered yield from the Fe atoms, compared to that for an unimplanted crystal (see Table II). The absence of any distinct damage peak in the aligned spectra (Figs. 6 and 7) indicates that the increased yield arises principally from dechanneling caused by displaced lattice atoms, and that any direct scattering contribution is small.[24] It is seen from Table II that the level of damage is low and increases slightly with increasing Br dose. The damage could have been reduced by subsequent annealing of the crystals. However, it will be seen in Sec. VII that this induces precipitation of the Br atoms.

Radiation damage caused by the ^{4}He and ^{14}N analyzing beams was found to be negligible compared to that resulting from the Br implantation. Even after a dose of ~ 100 μC of ^{14}N ions (over an area ~ 1 mm^2) in a particular scan, no change could be detected in the aligned Fe yield.

B. Possible enhanced diffusion of N in Fe

An interesting effect observed in a preliminary {211} planar scan performed with 3.5-MeV ^{14}N is shown in Fig. 11. The two scans were carried out two weeks apart, with the beam incident on the same position on the crystal. Although the number of points in the first scan is insufficient for the Br double peak to be resolved, in the second scan the central Br peak is considerably enhanced with respect to the first. (The Fe minimum yield is higher than in Fig. 9, owing to poorer surface preparation.) This change indicates that at least some of the Br atoms have moved to a new site in the crystal in the period between the two scans.

A possible explanation of this effect in terms of enhanced diffusion of N in Fe has already been given.[25] The effect was only observed when the analyzing beam was incident on a beam spot that had already been bombarded with N two weeks previously. For each measurement used in the determination of the Br location a new beam spot was chosen. During a 30-h angular scan the individual points were always reproducible, indicating that the location did not change in this time. This is further substantiated by the Br χ_0 values in Table II, where good agreement is observed between the ^{14}N and ^{4}He results for the same channel.

VI. INTERPRETATION OF RESULTS

A. Qualitative

The narrow width of the {100} flux peak (Fig. 9), and its magnitude relative to the dip on which it is superimposed, indicate that a substantial fraction of the Br must occupy interstitial sites in the center of a {100} planar channel. At the same time some of the Br must be in positions well displaced from the center to produce the dip under the peak.

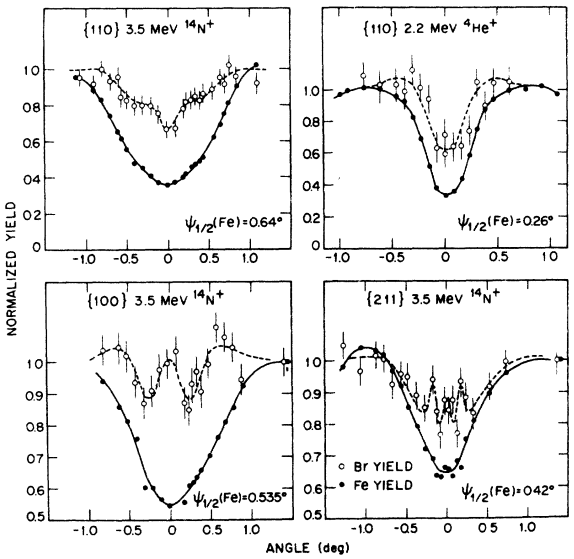

FIG. 9. Angular scans across {110}, {100}, and {211} planes. The details are the same as for Fig. 8.

TABLE III. Orientation of tilting planes for the experimental angular scans (Figs. 8 and 9), and for the computer simulated scans (Sec. VI B).

Channel	Analyzing beam[a]	Energy (MeV)	Tilting plane[b] (experimental scan)	Tilting plane[b] (computer simulation)
⟨111⟩	He	2.2	7° from {110}	14° from {110}
⟨100⟩	He	2.2	8° from {110}	14° from {110}
	N	3.5	20° from {110}	
⟨110⟩	N	3.0	9° from {100}	14° from {100}
{110}	He	2.2	20° from ⟨100⟩	8° from ⟨110⟩
	N	3.5	8° from ⟨110⟩	
{100}	N	3.5	8° from ⟨110⟩	8° from ⟨110⟩
{211}	N	3.5	9° from ⟨110⟩	8° from ⟨110⟩

[a]All of the computer simulations were carried out for He ions, of energy 2.2 MeV in the axial scans and 3.5 MeV in the planar scans.

[b]The tilting planes were chosen so as not to correspond to any major plane in the lattice.

From the discussion in Sec. II, the triple peak in the {211} scan implies that a certain fraction of the Br atoms is situated at the center of a {211} planar channel, while other atoms occupy a site displaced from the channel axis. The dip underneath the triple peak requires a further fraction of the Br to be lying close to the channel walls. Equation (2) is used to deduce the position of the atoms which give rise to the double peak; multiple scattering is sufficiently small in this case to be neglected. The angular position of the double peak ($\psi_i = 0.16° \pm 0.03°$) must first be multiplied by the ratio of the calculated critical angle for a {211} plane (see Sec. VI B) to the experimental value $\psi_{1/2}$(Fe). Using a Lindhard planar potential[12] (including contributions from both planes bounding the channel) we obtain

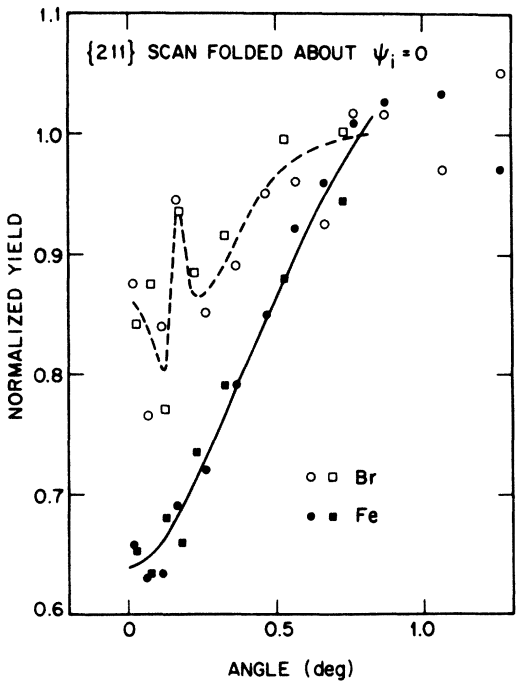

FIG. 10. The {211} planar scan in Fig. 9 folded about the center, to emphasize the triple-peak structure. The circles denote data points for $\psi_i \leq 0$ in Fig. 9, the squares points for $\psi_i > 0$. In this case the smooth curve through the Br data is drawn to pass through the values obtained by averaging adjacent points in pairs.

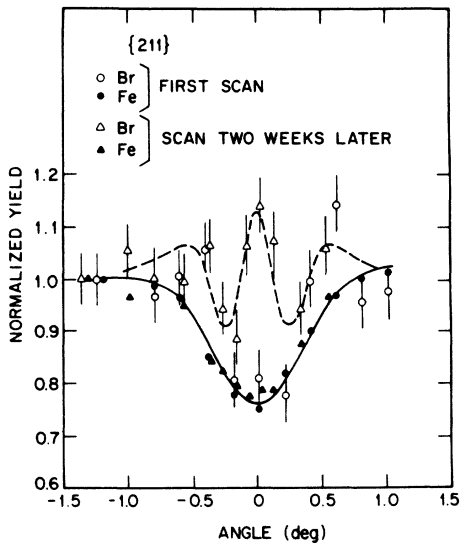

FIG. 11. Two {211} planar scans for 3.5-MeV $^{14}N^+$ ions. The second scan was carried out two weeks after the first, with the beam incident on the same position on the crystal. The smooth curves through the data points are only to guide the eye.

$\rho_d = 0.16 \pm 0.04 d_p$, where ρ_d is the distance from the channel center and d_p is the interplanar spacing.

It is necessary at this point to make a restriction on the symmetry of the allowed Br sites. Whichever position is selected in a particular {211} planar channel to correspond to the double peak, there will be a distribution of positions across the channel when all physically equivalent sites are taken into account. The magnitude and narrow angular width of the twin peaks imply a high concentration of atoms in a small number of discrete positions. Therefore we choose sites of the highest possible planar symmetry consistent with $\rho_d/d_p = 0.16 \pm 0.04$. Of the various possible values we take $\rho_d/d_p = \frac{1}{8}$ (0.125), as the equivalent sites in this case occupy only four distinct positions across a {211} channel (at $\frac{1}{8}d_p$, $\frac{1}{4}d_p$, $\frac{3}{8}d_p$ and $\frac{1}{2}d_p$ from the channel axis; cf. Fig. 14). For values such as $\frac{1}{6}$ (0.17) or $\frac{3}{16}$ (0.19) the distribution of equivalent sites is more diffuse, especially near the center of the channel. [It can be shown that sites lying at the center of a {100} planar channel have the highest symmetry in {211} channels for $\rho_d/d_p = (\frac{1}{2})^n$, where n is the lowest integer for which ρ_d/d_p is compatible with the data; here $n = 3$.]

We now have the following constraints:

(i) A substantial fraction of the Br atoms must lie at the center of a {100} planar channel.

(ii) The distribution of the atoms across a {211} channel must be heavily concentrated at the center, and on planes $\frac{3}{8}$ and $\frac{5}{8}$ of the distance across the channel (at $\pm \frac{1}{8}d_p$ from the center).

(iii) Since no flux-peaking effects are observed for any of the three axes or the {110} plane, there can be no sites situated at the center of ⟨111⟩, ⟨100⟩, or ⟨110⟩ axis channels or {110} planar channels. (This condition immediately excludes the usual octahedral and tetrahedral interstitial sites in the Fe lattice.[8,11])

A systematic search for interstitial sites that satisfy these constraints can be made by using simple symmetry arguments. For a particular site, the projections of the various physically equivalent sites on a plane perpendicular to a particular axial (or planar) direction are identical to the positions of one site viewed along the various equivalent axial (or planar) directions.[26] Thus if we take a plane at the center of a particular {100} channel, and consider the intersection with this plane of the various equivalent lines and planes on which Br atoms are either allowed or forbidden to lie by constraints (ii) and (iii) above, all possible Br sites will be determined.

Figure 12(a) shows the intersections of all equivalent {211} channel center and $\frac{3}{8}$, $\frac{5}{8}$ planes with that portion of a {100} center plane cut off by a unit cell. Allowed Br sites are situated at the intersections within this plane of the {211} center plane lines with the $\frac{3}{8}$, $\frac{5}{8}$ plane lines. Also plotted are the intersections with the plane of lines lying along the centers of all equivalent ⟨111⟩, ⟨100⟩, and ⟨110⟩ axial channels, and planes lying at the center of {110} planar channels. These define sites forbidden to the Br atoms (though, in fact, no points allowed by the {211} constraint lie on the forbidden lines). It is seen that there is quite a large number of allowed sites. However, by invoking the symmetry argument used earlier, all but three of these can be rejected. The remaining three sites, which we designate the X, Y, and Z sites, respectively, are shown in Fig. 12(b). In all other cases (for example, the point $(\frac{7}{24}, \frac{7}{24})$ with respect to a corner of the square, and equivalent positions), the distribu-

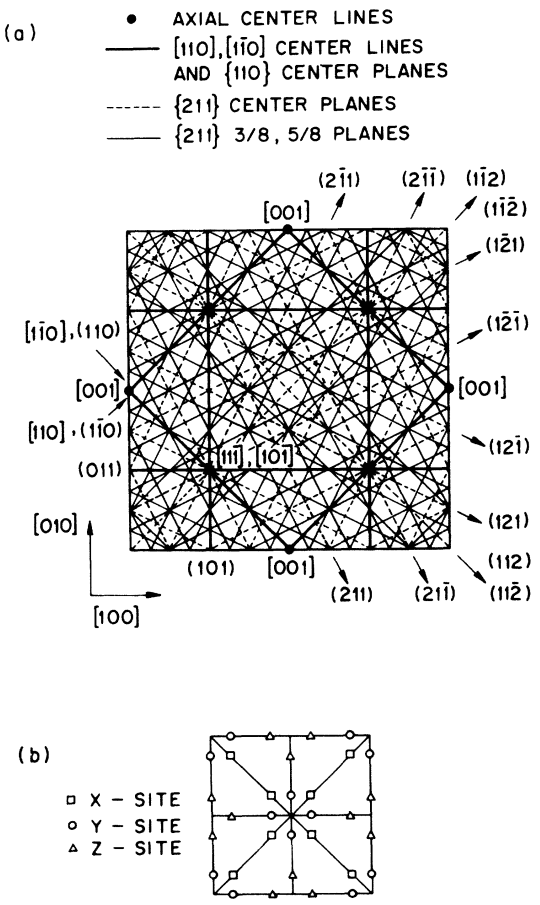

FIG. 12. Illustrating the constraints on the interstitial sites in the Fe lattice occupied by the Br atoms. The area shown is that portion of a {100} channel center plane cut off by a unit cell. (a) Forbidden sites (axial channel center lines and {110} channel center planes) and allowed sites (intersection of {211} channel center planes and $\frac{3}{8}$, $\frac{5}{8}$ planes). The lines corresponding to the (112) and (11$\bar{2}$) planes coincide, as do those for the (1$\bar{1}$2) and (1$\bar{1}\bar{2}$) planes. (b) Positions of the allowed X, Y, and Z sites in the area in (a).

tion of equivalent sites across a {211} channel is too diffuse to produce a sharp double peak.

The location of the X, Y, and Z sites in the Fe unit cell can be seen more clearly in Fig. 13. The three sites respectively occupy positions such as $\frac{3}{8}\frac{3}{8}\frac{1}{4}$, $\frac{3}{4}\frac{3}{8}\frac{1}{2}$, and $\frac{1}{8}\frac{1}{4}\frac{1}{2}$. For each site there are altogether 48 physically equivalent positions per unit cell; for any general site in the bcc lattice there are 96 equivalent positions per unit cell (containing two lattice atoms). The location of the octahedral and tetrahedral sites is included in Fig. 13 for comparison.

Figure 14 shows the projections of the various physically equivalent X, Y, and Z sites on planes perpendicular to the major axial and planar channels (projections for the tetrahedral site are included). All three sites are consistent with the three constraints above, and are thus qualitatively consistent with the data. To place the interpretation on a quantitative basis, calculations of the angular yield curves for atoms in these sites are required.

B. Yield calculations

Theoretical angular-yield curves for a particular site can be calculated from the flux distribution profiles, as a function of the angle of incidence, for each channel. Two types of calculation were carried out to determine flux profiles: (a) Monte Carlo computer simulations[2,11] based on a binary-collision model, and (b) analytical calculations based on the average potential model.[12]

The calculations are complementary. An analytical model has the advantage of simplicity; however, the implicit assumption of statistical equilibrium in the transverse plane precludes consideration of depth oscillations in the channeled flux distribution.[1,14,27] Nuclear and electronic multiple scattering cannot be readily incorporated in the model. These factors are easily taken into account in a computer simulation, and other conditions (such as the beam divergence) can be readily varied. However, considerable computation time is required to follow the individual particle trajectories.

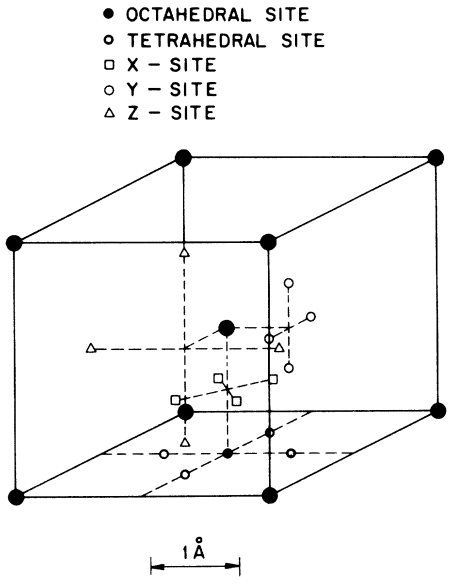

FIG. 13. Location of the X, Y, and Z interstitial sites in the bcc Fe unit cell. The large filled circles represent Fe atoms. Only four of the 48 physically equivalent sites are shown in each case. The positions of one of the three equivalent octahedral sites and four of the 12 equivalent tetrahedral sites are also shown.

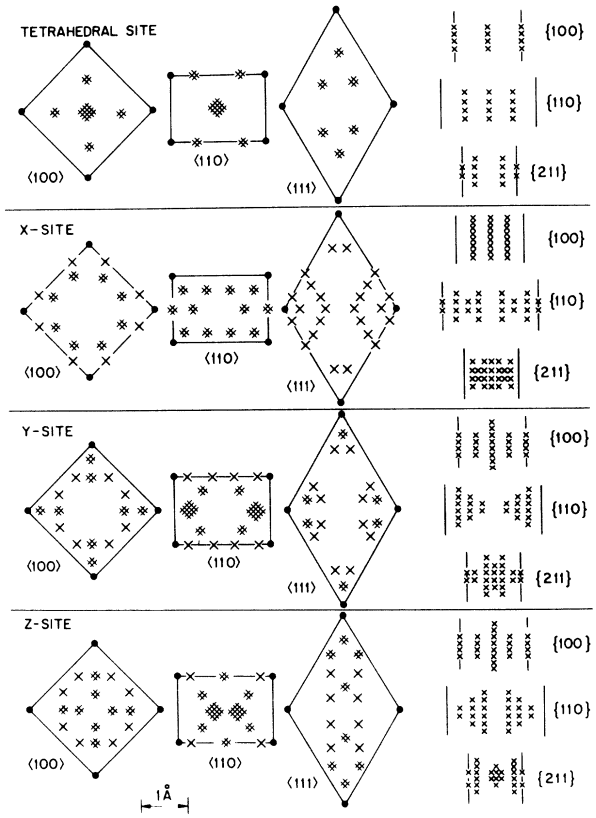

FIG. 14. Projections of the various physically equivalent X, Y, and Z sites on planes normal to ⟨111⟩, ⟨100⟩, and ⟨110⟩ axial channels and {110}, {100}, and {211} planar channels in Fe. Filled circles in the case of the axes and lines in the case of the planes denote rows and planes of Fe atoms, respectively. Each cross represents two physically equivalent sites. In each channel, the sites lie on a set of grid lines spaced $\frac{1}{8}$ of a channel dimension apart, except for the Z site in the ⟨111⟩ channel where the spacing is $\frac{1}{16}$. The tetrahedral site is included for comparison (each cross representing only one equivalent site).

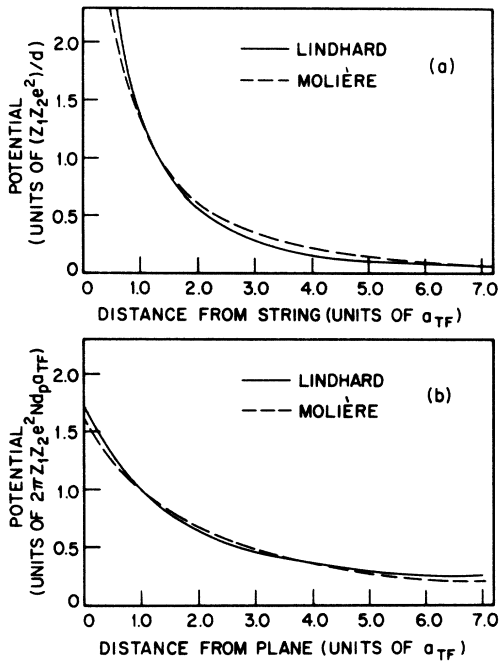

FIG. 15. Comparison of the Lindhard potential (Ref. 12) and the average potential derived from the Molière approximation to the Thomas-Fermi potential (Ref. 31), both in a static lattice, for (a) a single atomic row (string), and (b) a single plane. The symbols in which the scale units are expressed are defined in the Appendixes.

Details of the two models are given in the Appendixes. The Monte Carlo simulations are essentially the same as those carried out by other authors[14,28,29] in a variety of channeling studies. The analytical calculations are similar to those of Andersen[30] and Picraux *et al.*,[10] but give the flux distribution profile (across a channel) for an external beam of ions rather than the emergent angular distribution of ions originating within the crystal. For the computer simulations the Molière approximation to the Thomas-Fermi potential[31] was used, while the analytical calculations employed the standard Lindhard row and plane potentials. In Fig. 15 the corresponding average potentials are compared; for both rows and planes, the two potentials agree closely over a wide range of impact parameters.

The Monte Carlo simulations were carried out with ^{4}He ions, the energies being 2.2 and 3.5 MeV for the axial and planar scans, respectively. It was established in several cases that the flux profile for ^{14}N ions was the same as that for ^{4}He (within the limits of statistical accuracy). The beam divergence in all scans was ±0.045°, which included an allowance for multiple scattering[32] in the surface oxide layer (≈ 35 Å thick). Multiple scattering associated with electrons is incorporated in the model. The temperature was taken as 20 °C, and the flux distributions were averaged over a depth of 500 Å from the crystal surface (cf. $\bar{R}_p$ = 270 Å for the implanted Br). Tilting planes for the angular scans are included in Table III. The simulations were performed with the Harwell IBM 360/75 computer.

In the analytical calculations the particles and energies chosen were the same as those used experimentally. The model does not include beam divergence or thermal vibrations of the lattice atoms. A PDP-8 computer was used for these calculations.

In both sets of computations, fluxes were averaged over the area of a square (axial channels) or strip (planes) of dimension ≈ 0.14 Å (cf. x_{rms} = 0.061 Å in Fe at 20 °C); this allows in a simple way for thermal vibrations of the Br atoms. The flux was always normalized to the random value. The accuracy of the calculations depends on the initial number of particles in the case of the computer simulations, and on the numerical integration interval in the analytical case. An improvement in accuracy can be achieved by taking advantage of both channel and site symmetry. Typical errors for each angular point in the calculated scans were ~ 3%. To obtain the Br angular-yield curves in Sec. VI C, smooth curves were drawn through the individual points.

The curves (dips) for the Fe lattice atoms were determined by calculating the flux within a distance $r_{crit} = a_{TF}$ [Eq. (A2)] of the atomic rows or planes. It might be more appropriate to take $r_{crit} = (a_{TF}^2 + u^2)^{1/2}$, where u is the rms thermal vibrational amplitude perpendicular to a row or plane. However, in this case a_{TF} (= 0.146 Å for ^{4}He in Fe) is sufficiently large compared with $u(u_{axial}$ = 0.086 Å, u_{planar} = 0.061 Å at 20 °C) that taking $r_{crit} = a_{TF}$ is a reasonable approximation. It was found that the exact choice of r_{crit} had little effect on the Fe dips for planar channels, while for the axes there was only a significant effect for angles $\gtrsim \psi_{1/2}$.

C. Quantitative

The yield calculations take into account implicitly the random fraction of the incident beam arising from transmission through the crystal surface. Before the calculations can be compared with the experimental data, an allowance must be made for the additional random fraction due to dechanneling in the damaged Fe lattice. It is assumed (cf. Sec. V A) that any direct scattering of the channeled beam by displaced Fe atoms is negligible in comparison with dechanneling.

The random fraction of the incident beam associated with surface transmission is given by the cal-

culated Fe yield $\chi_{Fe}^{calc}(\psi)$, where ψ is the angle of incidence. The additional random fraction is

$$f_R'(\psi) = f_R [\, 1 - \chi_{Fe}^{calc}(\psi) \,], \tag{3}$$

f_R being the fraction of the initially channeled part of the beam that has become dechanneled (random) at the depth of the Br; f_R is given by

$$f_R = \frac{\chi_{Fe}^{exp}(0) - \chi_{Fe}^{calc}(0)}{1 - \chi_{Fe}^{calc}(0)}, \tag{4}$$

in which $\chi_{Fe}(0)$ is the same as $\chi_0(\mathrm{Fe})$ defined earlier and the superscripts denote the experimental and calculated values, respectively. Because of the assumption above, this equation may slightly overestimate f_R. Typical values of f_R were 0.05 for axes and 0.2–0.4 for planes. For nonsubstitutional Br atoms, the calculated yield $\chi_{Br}^{calc}(\psi)$ corrected for the additional random fraction is then

$$\chi_{Br}^{corr}(\psi) = (1 - f_R)\chi_{Br}^{calc}(\psi) + f_R = \chi_{Br}^{calc}(\psi) + f_R[1 - \chi_{Br}^{calc}(\psi)]. \tag{5}$$

Clearly the correction is only appreciable for large values of f_R and for values of $\chi_{Br}^{calc}(\psi)$ which differ significantly from 1. The yield curves for Br atoms in substitutional sites will be the same as the experimental Fe curves, if it is assumed that the Br and Fe atoms have the same mean thermal vibrational amplitude; that is,

$$\chi_{Br}^{corr}(\psi) = \chi_{Fe}^{exp}(\psi), \tag{6}$$

where $\chi_{Fe}^{exp}(\psi)$ is the experimentally measured Fe yield. All the Br curves presented in this section were computed using Eqs. (5) and (6).

In Fig. 16 the results of analytical calculations for the X, Y, and Z sites in a {211} planar channel are illustrated. For the Z site, the double peak (on either side of the central peak) is considerably lower in magnitude than for the X or Y site. This is due to the weak concentration of equivalent sites on the $\frac{3}{8}$, $\frac{5}{8}$ planes in the channel, compared to the other two sites (Fig. 14). (The pronounced shoulders near the extremes of the scan are due to the high concentration of equivalent sites close to the edges of the channel.) As a strong double peak is observed experimentally, the Z site is rejected and only X and Y sites are considered further.

Comparisons between the calculated Br-yield curves for the X and Y sites and the six experimental angular scans are presented in Fig. 17 and 18, respectively; the angular scale is normalized to $\psi_{1/2}(\mathrm{Fe})$ in each case. The essential features of the Monte Carlo and the analytical curves are seen to be the same. Differences are due partly to the different potentials and partly to multiple scattering and depth effects which are not included in the analytical model.

It is clear from Figs. 17 and 18 that if all the Br atoms are assumed to be either in site X or site Y, or distributed between the two sites, the calculations are not consistent with the measurements. In the axial scans, the calculated curves show dips that are narrower than those observed experimentally and the magnitude of the yields is too high. For the planes, the basic features of the data are reproduced, but again the yields are too high.

Since the calculated yields are all higher than the experimental values, we have been led to consider admixtures of both X and Y sites with a substitutional component; sites displaced by a distance $\approx a_{TF}$ (in various directions) from substitutional positions were also considered. It was assumed that the atoms were distributed between only two different equilibrium sites (for example, distributions among X, Y, and substitutional sites were not considered). Figure 19 shows computations for a distribution of 50% of the Br in the X interstitial site and 50% substitutional. The agreement with the measurements is seen to be much better than in Fig. 17; however, except for the {211} plane the calculated yields are slightly too low. Similar results (not shown) are obtained in the case of the Y site.

The two distributions that produce the best agreement with the experimental data are (i) 67% Y, 33% substitutional; (ii) 60% X, 40% substitution-

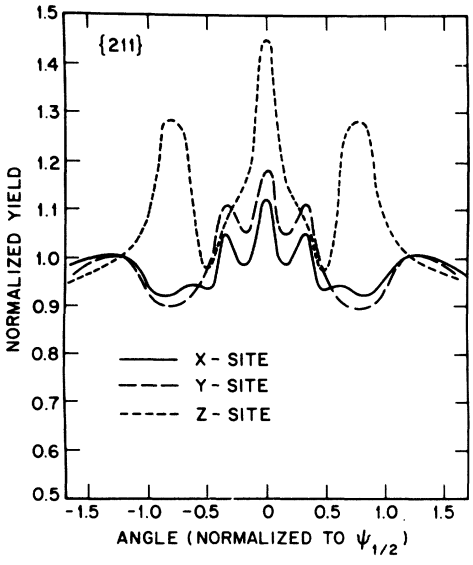

FIG. 16. Analytical calculations of the angular-yield curves for Br atoms in the X, Y, and Z sites, respectively, in a scan across a {211} planar channel in Fe. The computations were performed for 3.5-MeV ^{14}N ions, and the angular scale is normalized to the calculated value of $\psi_{1/2}(\mathrm{Fe})$. The effect of the random fraction of the incident beam arising from dechanneling in the damaged Fe lattice [Eqs. (5) and (6)] is incorporated in the calculations.

al. Calculations for these two cases are shown in Figs. 20 and 21, respectively.

In the axial scans, both the features and the yields favor case (ii) except in the ⟨100⟩ scan near $\psi = \psi_{1/2}$, where better agreement is obtained for case (i). However, good agreement between calculation and experiment is not necessarily expected in the region near $\psi_{1/2}$, where the calculated Fe

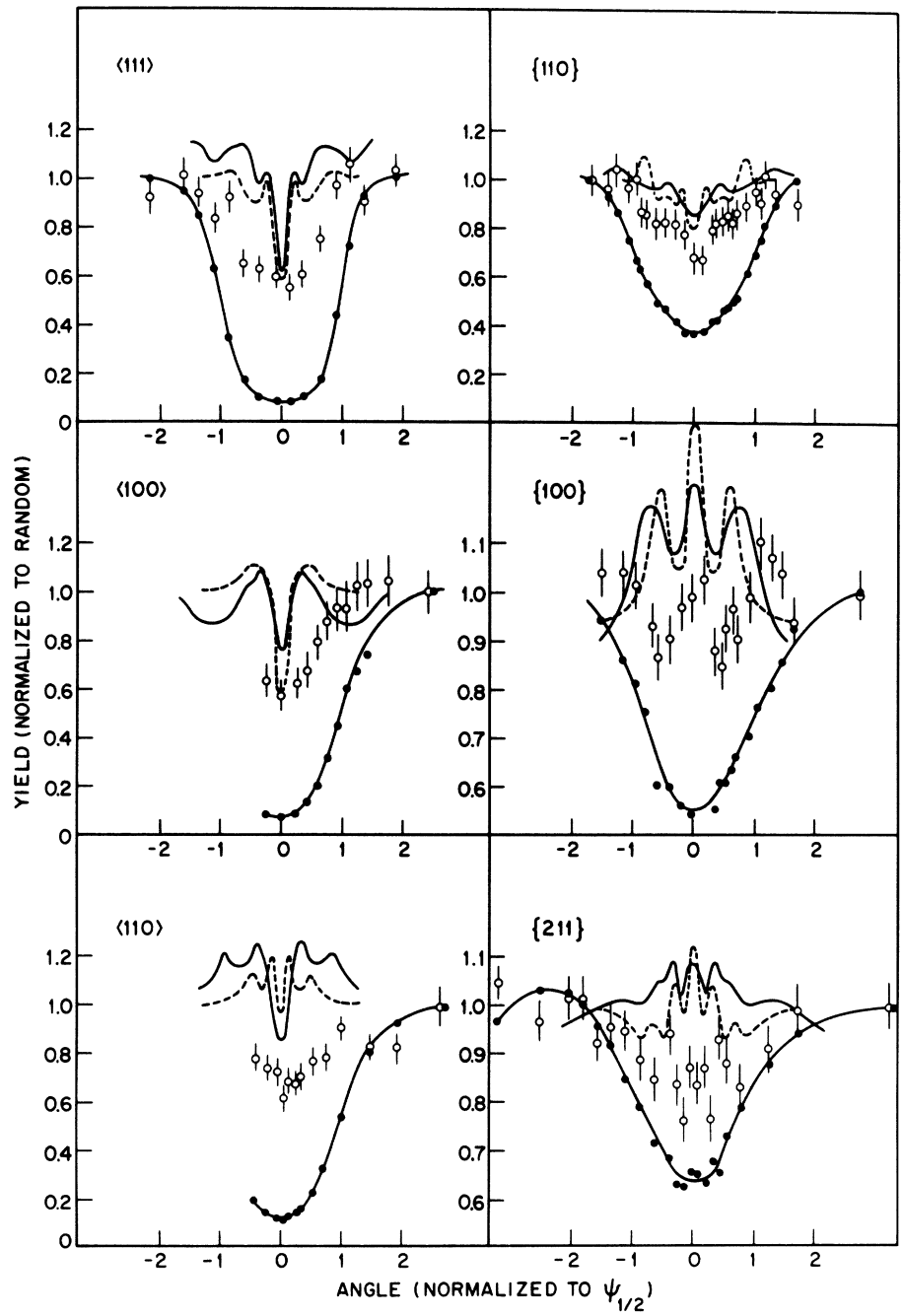

FIG. 17. Comparisons between the calculated yield curves and the experimental angular scans (Figs. 8 and 9) for Br atoms in the X interstitial site. The ⟨100⟩ and {110} scans carried out with ^{4}He ions are not included. The solid lines are for the Monte Carlo simulations, the dashed lines for the analytical calculations (the solid lines through the Fe points are only to guide the eye). In each scan the angle is normalized to $\psi_{1/2}$(Fe). The effect of the random fraction of the incident beam arising from dechanneling in the damaged Fe lattice [Eqs. (5) and (6)] is included in all cases.

dips are uncertain owing to the choice of r_{crit} (Sec. VIB). In the {110} planar scan, the features are similar in both cases but the calculated yield favors (i). For the {100} plane better agreement is obtained in case (ii); the double peak (shoulder) near the extremes of the scan in both sets of calculated curves is not observed experimentally. In the {211} scan the triple-peak structure is reproduced for both distributions, though it is slightly more pronounced in case (i). On the other hand, the yield is in better agreement with the data for case (ii). (We note here that the Br χ_0 result for the {111} plane in Table II is consistent with both these possibilities.)

It is believed that the difference between the calculated and experimental double peak in the {211}

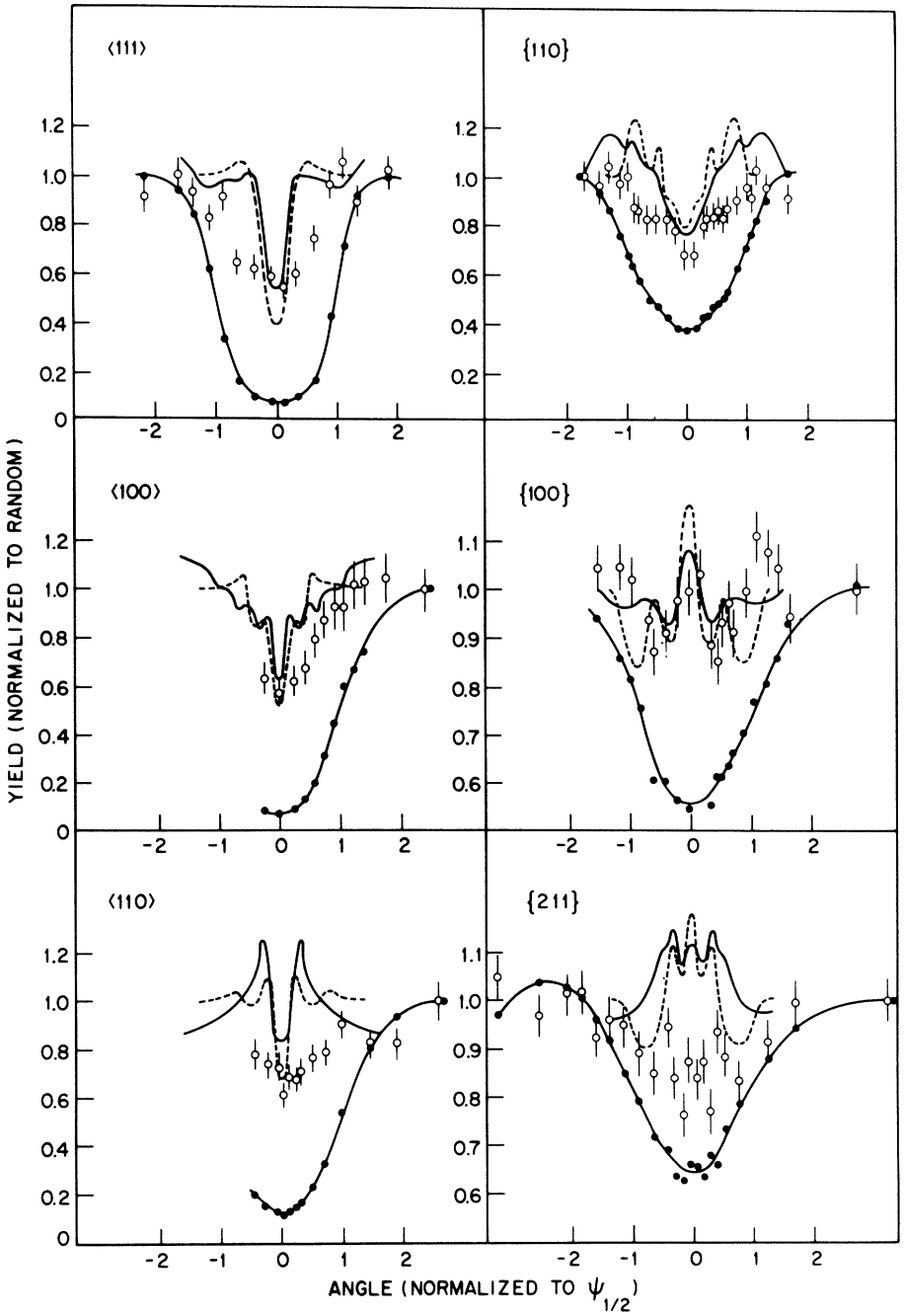

FIG. 18. As in Fig. 17, for Br atoms in the *Y* interstitial site.

scan (for both distributions) can be attributed to the potentials used in the calculations. The magnitude and width of the twin peaks depend directly on the magnitude of the second derivative (that is, the flatness) of the transverse potential near the center of the channel.[5] The difference between the Monte Carlo and analytical curves for the {211} scan is due largely to the different potentials used in the two sets of calculations (cf. Fig. 15). A more pronounced double peak would be obtained if the potential were flatter than the average Molière or Lindhard potentials near the channel center. Planar channeling experiments[33,34] in Au and Si indicate that actual planar potentials are indeed somewhat flatter than these two potentials.

The distribution selected is 60% of the Br atoms in the X interstitial site and 40% substitutuional, as this gives better over-all agreement with the data

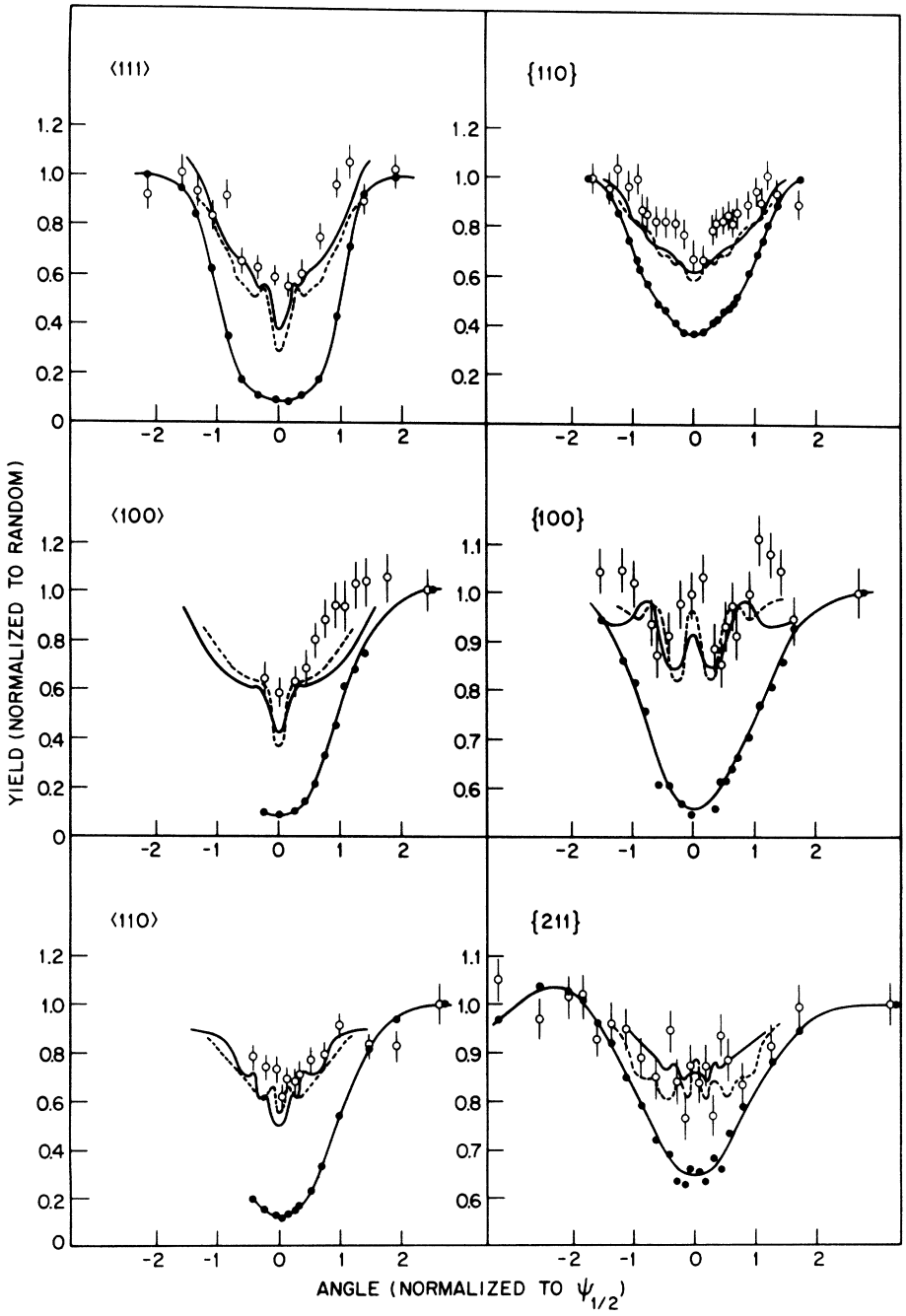

FIG. 19. As in Fig. 17, for a distribution of 50% of the Br in the X site and 50% substitutional.

than the 67% Y, 33% substitutional distribution. Changes of only 5% in these numbers result in somewhat poorer agreement with the data, showing the sensitivity of the calculations.

Finally, the Br χ_0 results in Table II for the low- and high-dose implants are compared with those for the implantations at 5×10^{14} ions/cm^2 (the dose for the angular scan measurements). Within the limits of experimental error, the results are the same, indicating that the Br location is independent of concentration in the range from 1×10^{14} ions/cm^2 (local concentration 0.07 at.%) to 5×10^{15} ions/cm^2 (local concentration 3.5 at.%).

VII. ANNEALING MEASUREMENTS

In order to correlate the location results with hyperfine-interaction data, additional measurements were made on a crystal annealed after im-

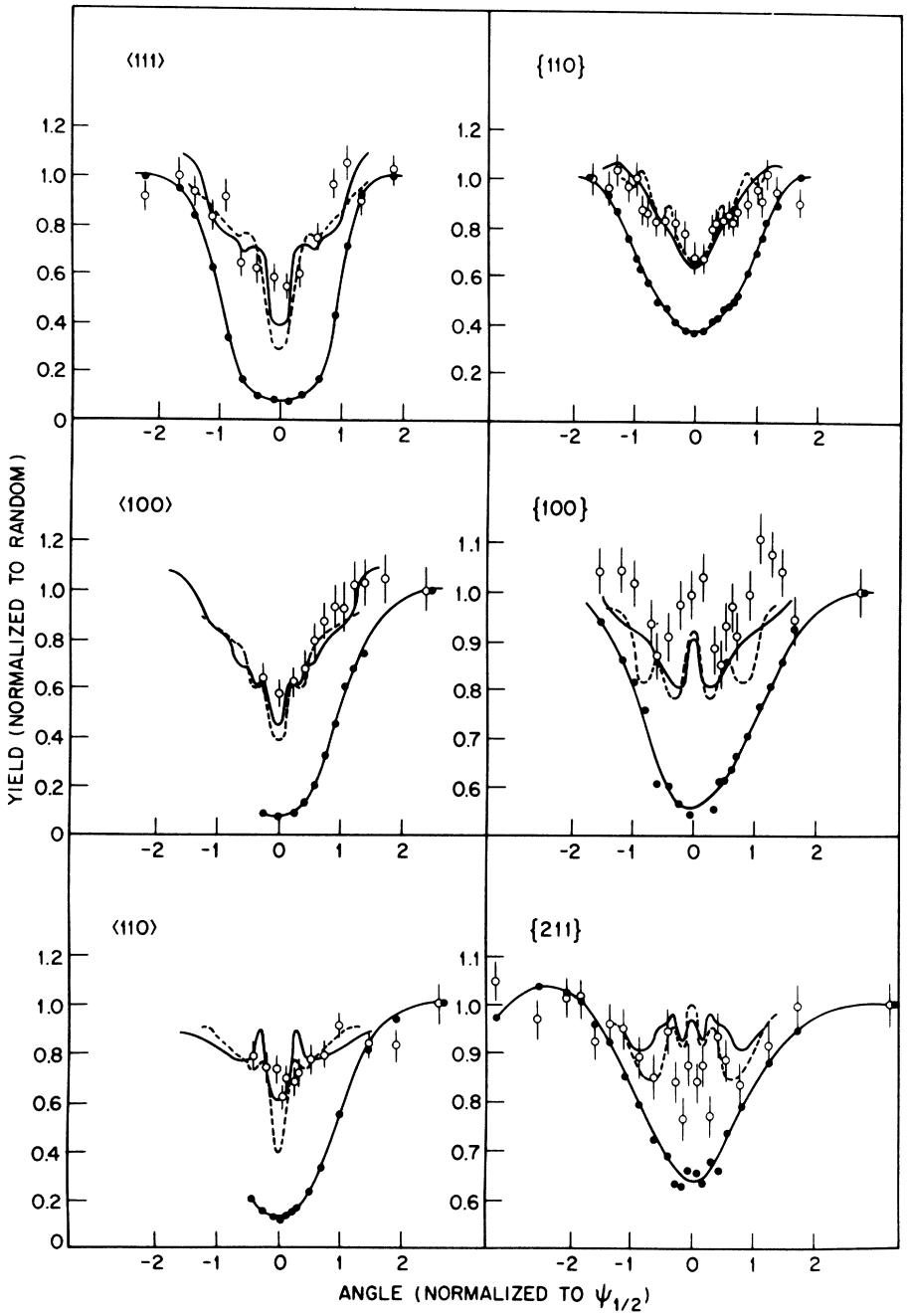

FIG. 20. As in Fig. 17, for a distribution of 67% Br in the Y interstitial site and 33% substitutional.

plantation. The crystal was annealed for 30 min at 600 °C in an evacuated quartz tube (pressure $\lesssim 10^{-7}$ Torr).

The results of an angular scan across a ⟨111⟩ axis in the annealed crystal are presented in Fig. 22. The Br yield is independent of angle and is equal to the random value (whereas the scan for the unannealed crystal shows a substantial dip). For the ⟨100⟩ axis a value of χ_0 (Br) = 1.00 ± 0.08 (Table II) was obtained. These results indicate that the Br atoms no longer occupy any specific crystallographic site following the annealing. Comparison of the spectra for annealed and unannealed crystals showed that the annealing had been accompanied by a migration of Br towards the surface of the Fe, and that there had been a loss of approxi-

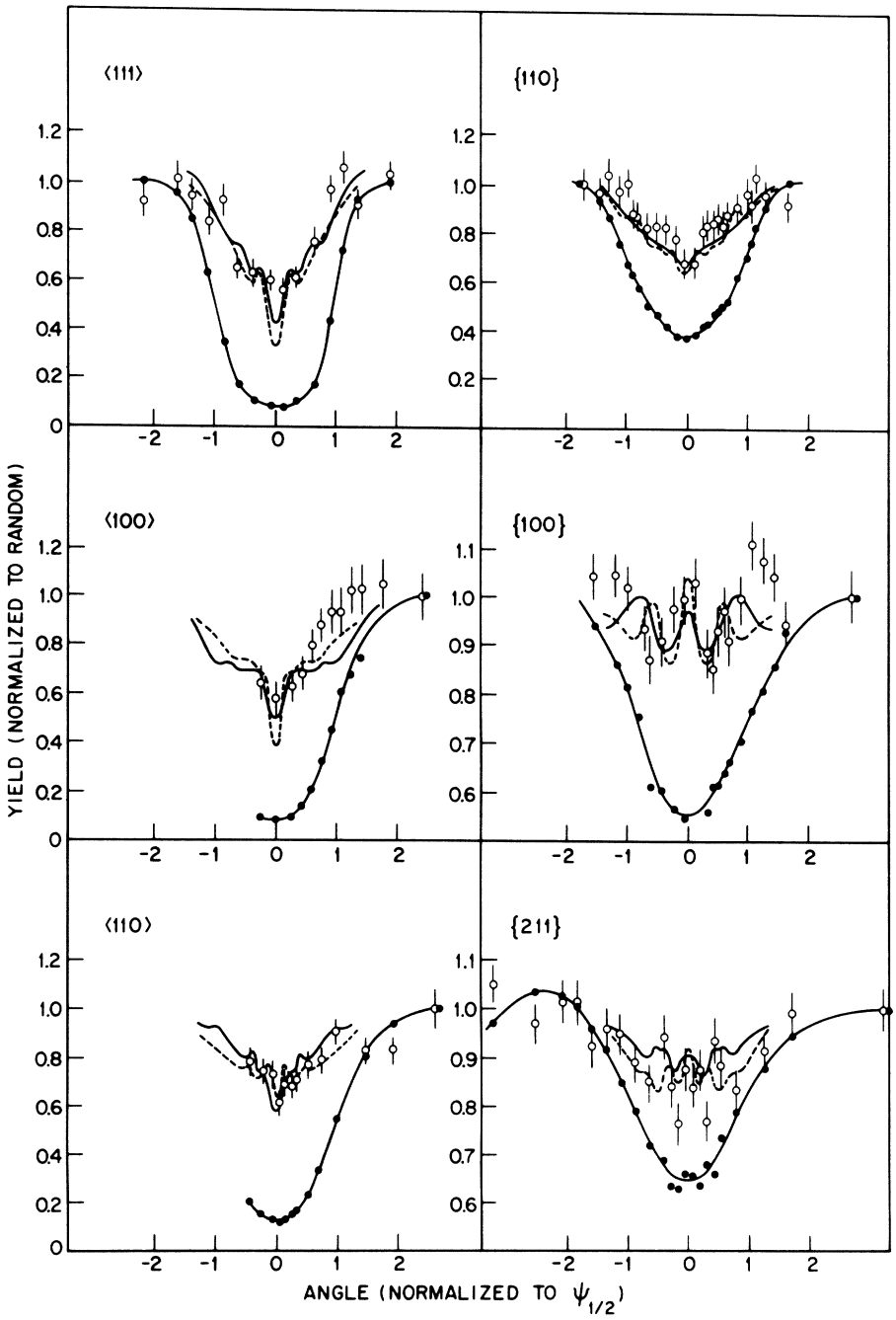

FIG. 21. As in Fig. 17, for a distribution of 60% Br in the X interstitial site and 40% substitutional.

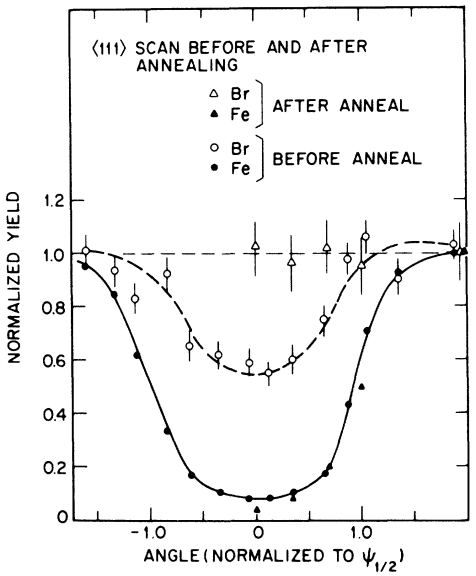

FIG. 22. Angular scans across a ⟨111⟩ axis in a Br-implanted Fe single crystal, before and after a 600 °C anneal. The two scans were performed with 2.2-MeV $^4He^+$ and 3.5-MeV $^{14}N^+$ ions, respectively, and in each case the angular scale is normalized to $\psi_{1/2}$(Fe).

mately 50% of the Br from the crystal. It is concluded that precipitation or clustering of the Br occurs at temperatures $\lesssim 600\,^\circ C$.

VIII. DISCUSSION

The results of this study illustrate some of the possibilities of the channeling technique for atom location. From the structure observed in the planar scans, it has been possible to specify a maximum of three interstitial sites (of low symmetry) qualitatively consistent with the data. A quantitative interpretation has been made using theoretical calculations of angular-yield curves. To fit the data, it has been necessary to consider distributions of Br atoms between the X or Y interstitial sites (Fig. 13) and substitutional (or nearly substitutional) sites in the Fe lattice. Only distributions between two sites have been considered. The best agreement between the calculated yield curves and the measurements is obtained for 60% of the Br in the X site and the remaining 40% substitutional.

Qualitative agreement is obtained between the yield curves from the Monte Carlo computer simulations and the analytical model. Similar agreement has been found previously for atoms in substitutional sites in axial channeling calculations.[35] Depth oscillations in the channeled flux distributions appear to have only a small effect on the magnitude of the calculated yields. This is probably because the average value of the flux over 500 Å from the crystal surface (at a particular point in the channel) is not too different from its equilibrium value.

One of the main experimental limitations in this type of experiment is the background in the backscattered energy spectra arising from pulse pileup. An alternative process to backscattering in atom location studies is the ion-induced production of characteristic inner-shell x rays. However, preliminary measurements of the ion-induced x-ray yield from Br in Fe revealed severe background problems associated both with pileup of the characteristic Fe x-ray pulses and with other effects.

It is of interest to consider how the proposed location of the Br atoms might originate. The proximity of the X site to a lattice site (Fig. 13), and the large size of the Br atom (singly charged ionic radius 1.95 Å[36]), almost certainly require that the adjacent Fe atom be displaced. (The same is true for the Y site.) One possibility is that some type of crowdion or split-interstitial configuration is formed by a Br atom in the X site and the displaced Fe atom.

Another possibility[37] is that some or all of the Br is present in the Fe lattice in the form of a coherent precipitate. A coherent precipitate[38] is a distribution of small local precipitates of a chemical phase or compound (such as $FeBr_3$), each oriented in the same way with respect to the host lattice. It is a metastable phase, formed under certain conditions when the local concentration of solute atoms exceeds the solid solubility limit in the host (the solubility of Br in Fe is not known). The formation of such a precipitate might explain why a large fraction of the Br occupies such an unusual interstitial site. Since the phase could persist over quite a large concentration range, the apparent lack of dependence of the Br location on concentration in the range 0.07–3.5 at.% is consistent with such a picture. In addition, complete precipitation or segregation of the Br on annealing might be expected. The existence of a coherent precipitate could be investigated by electron microscopy, as has been done for other implanted systems,[39] but this would require a concentration of Br atoms much higher than in this study.

A third possible explanation of the location is that the interstitial component is associated with vacancies, as suggested by de Waard[40] in the interpretation of Mössbauer-effect measurements on other implanted systems. If one or more vacancies are created (during implantation) in the vicinity of a Br atom initially on a lattice site, the Br atom will tend to move away from the site to a new equilibrium position. Some relevant results have recently been obtained[41] in a Mössbauer study of ^{125}I implanted into Fe. Analysis shows that 40% (± 5%) of the I nuclei occupy sites (probably substitutional) in which they experience a high magnetic hyperfine

field, while the remaining 60% are distributed between intermediate-and low-field sites. A similar result is obtained for ^{133}Xe implanted into Fe. It is suggested that the intermediate- and low-field sites are associated with one and two vacancies, respectively. Lattice-relaxation calculations by Drentje andEkster[42] for Xe in Fe show that the two sites are similar to the present X and Y sites. The fraction of both I and Xe atoms in high-field sites (40%) is the same as the substitutional fraction of Br proposed here.

The location result has implications for nuclear orientation measurements of the hyperfine field at ^{82}Br implanted into Fe. These measurements[43,44] indicate an average magnetic field at ^{82}Br nuclei in Fe of $\bar{H}_{eff} = 400$ kOe, whereas the systematics of hyperfine fields at impurities in Fe suggest a value of $H_{eff} \approx 1000$ kOe. If the field for Br nuclei in X sites is zero, then the field at substitutional sites could be as high as expected. Alternatively, if the substitutional field is less than the anticipated value, the location results indicate a substantial field at the nonsubstitutional X site.

ACKNOWLEDGMENTS

Valuable discussions with W. L. Brown, G. Dearnaley, N. J. Stone, and J. U. Andersen are appreciated. We are indebted to G. Read for his help in crystal preparation, to W. Temple for performing the implantations, and to R. A. Boie and H. Lie for their assistance with the pileup-rejection electronics. We also thank the operating staffs of the Harwell 5-MV and Bell 2-MV accelerators for their willing cooperation. One of us (R. B. A.) acknowledges the support of a combined U. K. Science Research Council–Harwell E. M. R. Fellowship, one of us (P. T. C.) that of a Commonwealth Postgraduate Scholarship.

APPENDIX A: BINARY COLLISION MODEL (MONTE CARLO SIMULATIONS)

In this model the interaction between an energetic ion and the lattice atoms is treated as a series of independent two-body collisions described by classical mechanics. Such a treatment is valid provided the energy is sufficiently high and the scattering angles are not too small. The scattering angles are calculated using the momentum approximation. Each trajectory is made up of a series of straight-line segments between successive collisions, any localized curvature being neglected. Random numbers are used to select an initial position for the particle at the crystal surface, and to allow for beam divergence and multiple scattering.

The interatomic potential used was the Molière approximation to the Thomas-Fermi potential. This is given by[31]

$$V(r) = (Z_1 Z_2 e^2/r)(0.1e^{-6r/a_{TF}} + 0.55e^{-1.2r/a_{TF}} + 0.35e^{-0.3r/a_{TF}}), \quad \text{(A1)}$$

where Z_1 and Z_2 are the atomic numbers of the ion and target atom, respectively, e is the electronic charge, and a_{TF} is the Thomas-Fermi screening radius

$$a_{TF} = 0.885 a_0 (Z_1^{2/3} + Z_2^{2/3})^{-1/2}. \quad \text{(A2)}$$

Here a_0 is the Bohr radius of the hydrogen atom (0.529 Å).

Multiple scattering caused by thermal vibrations of the lattice atoms and by electrons is included in the model. Thermal vibrations are simulated by giving each lattice atom a displacement with coordinates chosen at random from a triangular approximation to a Gaussian distribution. This has the form

$$P(x) = (6^{1/2} x_{rms} - |x|)/6x_{rms}^2, \quad \text{(A3)}$$

in which x_{rms} is the rms thermal vibrational amplitude in one dimension. Values of x_{rms} can be computed from the Debye model (see, e.g., Ref. 30). The Debye temperature for Fe was taken as 470 °K.[45]

For electronic multiple scattering the model of Van Vliet[4] was used. With each atomic collision is associated a single electronic collision, which gives rise to an angular deflection calculated using the usual momentum-approximation approach to multiple scattering. In a single collision the deflection is

$$\Delta\theta \approx \left[\frac{m}{M_1 E}\left(-\frac{dE}{dx}\right)\Delta x\right]^{1/2}, \quad \text{(A4)}$$

where m and M_1 are the electron and ion masses, respectively, E is the ion energy, and $(-dE/dx)\Delta x$ is the electronic energy loss over the path Δx between successive collisions. The direction of $\Delta\theta$ is taken to be at random in the plane normal to the ion velocity. The stopping power $(-dE/dx)$ used in Eq. (A4) was taken as 0.5 of the random stopping power. (In calculating the energy loss along the path of the ion due to electronic collisions, a stopping power equal to the random value was assumed.)

The flux profile at a given plane normal to the channel direction is obtained by dividing the channel cross section into grid squares (axes) or strips (planes) and recording the number of particles passing through each square or strip. Typically, 625 particles were used for the axial scans and 100 for the planar scans.

APPENDIX B: AVERAGE POTENTIAL MODEL (ANALYTICAL CALCULATIONS)

The analytical calculations are based on the continuum model developed by Lindhard. The standard row and plane potentials in Ref. 12 were used: for

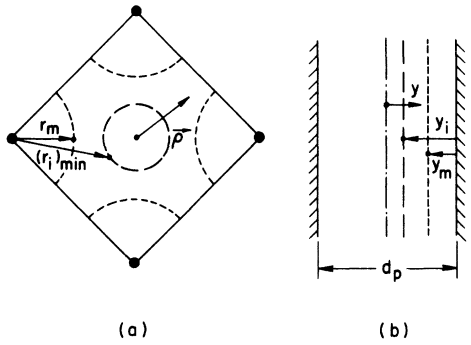

FIG. 23. Geometry for the continuum model calculations. (a) Cross section of an axial channel, showing the distances $(r_i)_{min}$ and r_m which appear in Eq. (B2). The dashed lines represent equipotential contours and the filled circles denote atomic rows. (b) Cross section of a planar channel, showing the distances y_i, y_m, and d_p in Eq. (B3). The dashed lines are equipotential lines and the solid lines denote atomic planes.

axial channeling, the average potential at a distance r from a single axial row is given by

$$U_1(r) = (Z_1 Z_2 e^2/d)\ln[(Ca_{TF}/r)^2 + 1], \qquad \text{(B1a)}$$

where Z_1, Z_2, e, and a_{TF} are as defined in Appendix A, C is a constant $\approx \sqrt{3}$, and d is the interatomic spacing along the particular axial direction. For planar channeling, the average potential at a distance y from a single plane is

$$Y_1(y) = 2\pi Z_1 Z_2 e^2 N d_p[(y^2 + C^2 a_{TF}^2)^{1/2} - y], \qquad \text{(B1b)}$$

where Nd_p is the atomic density of the plane.

In the continuum approximation the transverse energy of an ion at the crystal surface, $E_\perp = E\psi_i^2 + U(\vec{\rho}_i)$ [Eq. (1)], is conserved. Thus the subsequent trajectory of the particle is confined to that area of the transverse plane where $U(\vec{\rho}) < E_\perp$. A minimum distance of approach to a particular set of rows r_m (axial channeling) or to planes y_m (planar channeling) can then be defined. In calculating r_m for axial channeling only a single row was considered, since there is not a simple analytical solution for r_m when all rows bounding the channel are taken into account. For a single row, r_m is defined by

$$E\psi_i^2 + U_1(r_i)_{min} = U_1(r_m), \qquad \text{(B2)}$$

in which $(r_i)_{min}$ is the initial distance to the closest row [Fig. 23(a)]. The use of this equation is a good approximation except for low values of $E_\perp$; that is, for those ions entering the channel near the potential minimum with small values of ψ_i. It is these ions that largely determine the flux-peaking behavior. However, as no flux-peaking effects were observed in any of the axial scans, the error introduced by using Eq. (B2) is unimportant. For planar channeling, the solution for the closest distance of approach y_m, taking into account the two planes bounding the channel, is given simply by

$$E\psi_i^2 + Y_1(y_i) + Y_1(d_p - y_i) = Y_1(y_m) + Y_1(d_p - y_m), \qquad \text{(B3)}$$

with y_i and d_p as shown in Fig. 23(b).

Once statistical equilibrium has been achieved, the spatial probability distribution (and the transverse energy distribution) for an axially channeled ion is uniform within its accessible area. It is assumed that when $r_m \leq r_{crit} = a_{TF}$, the particle contributes only to the random fraction of the beam. Hence the probability for a particle with a minimum distance of approach to a row r_m to be at the position $\vec{\rho}$ (relative to the channel axis) is

$$\begin{aligned} f(\vec{\rho},\ r_m(E,\ \psi_i,\ \vec{\rho}_i)) &= 1/A(r_m), \quad |\vec{\rho}_j - \vec{\rho}| \geq r_m, \\ &\qquad r_m > a_{TF} \\ &= 0, \qquad |\vec{\rho}_j - \vec{\rho}| < r_m, \\ &\qquad r_m > a_{TF} \\ &= 1/A_0, \qquad r_m \leq a_{TF} \end{aligned} \qquad \text{(B4)}$$

where $A(r_m)$ is the area of the channel excluding the regions of radius r_m about each row, A_0 is the total channel area, and $\vec{\rho}_j$ is the position vector relative to the channel axis of the closest row. In cases where the excluded regions of radius r_m associated with different rows overlap, the magnitude of the area $A(r_m)$ is taken as that of the largest inscribed circle [though the shape of $A(r_m)$ is not changed]. The flux at the position $\vec{\rho}$ is

$$F(\vec{\rho}) = \int \int_{A_0} f(\vec{\rho},\ r_m(E,\ \psi_i,\ \vec{\rho}_i))\, dA(\vec{\rho}_i). \qquad \text{(B5)}$$

For planar channeling, the spatial probability distribution is not constant, as in axial channeling, but is inversely proportional to the square root of the transverse kinetic energy. In these calculations a simple harmonic distribution was assumed, as this has a particularly simple mathematical form. Such a distribution is a fairly good approximation in the central region of the channel, where flux-peaking effects are important. The probability of finding a particle with a minimum distance of approach to a plane y_m [Eq. (B3)] at a distance y from the center of the channel is then

$$\begin{aligned} f(y,\ y_m(E,\ \psi_i,\ y_i)) &= \frac{1}{\pi[(\frac{1}{2}d_p - y_m)^2 - y^2]^{1/2}} \qquad \tfrac{1}{2}d_p - y > y_m,\ y_m > a_{TF} \\ &= 0 \qquad \tfrac{1}{2}d_p - y < y_m,\ y_m > a_{TF} \\ &= 1/d_p \qquad y_m \leq a_{TF}. \end{aligned} \qquad \text{(B6)}$$

The singularity at $y = \frac{1}{2}d_p - y_m$ is removed by putting $y = \frac{1}{2}d_p - y_m - a_{TF}$ at this point. Again it is assumed that when $y_m \leq a_{TF}$, the particle contributes only to the random fraction of the beam. The flux is calculated from

$$F(y) = \int_0^{d_p/2} f(y,\ y_m(E,\ \psi_i,\ y_i))dy_i. \qquad \text{(B7)}$$

The integrals in Eqs. (B5) and (B7) are evaluated numerically. The integration interval chosen was of dimension a_{TF} (axes) or $\frac{1}{2}a_{TF}$ (planes).

---

*Work supported in part by a grant from the U. K. Science Research Council.

†Present address: Institute of Physics, University of Aarhus, Aarhus, Denmark.

[1]R. B. Alexander and J. M. Poate, Rad. Effects 12, 211 (1972).

[2]R. B. Alexander, G. Dearnaley, D. V. Morgan, and J. M. Poate, Phys. Lett. A 32, 365 (1970); R. B. Alexander, G. Dearnaley, D. V. Morgan, J. M. Poate, and D. Van Vliet, in *European Conference on Ion Implantation* (Peregrinus, Stevenage, England, 1970), p. 181.

[3]J. U. Andersen, O. Andreasen, J. A. Davies, and E. Uggerhøj, Rad. Effects 7, 25 (1971).

[4]D. Van Vliet, Rad. Effects 10, 137 (1971).

[5]M. A. Kumakhov, Rad. Effects 15, 85 (1972).

[6]B. Domeij, G. Fladda, and N. G. E. Johansson, Rad. Effects 6, 155 (1970).

[7]N. Iue, N. Matsunami, K. Morita, N. Itoh, M. Yoshida, and S. Hirota, Rad. Effects 14, 191 (1972).

[8]J. U. Andersen, E. Laegsgaard, and L. C. Feldman, Rad. Effects 12, 219 (1972).

[9]L. C. Feldman, E. N. Kaufmann, J. M. Poate, and W. M. Augustyniak, in *Proceedings of the International Conference on Ion Implantation in Semiconductors and other Materials, Yorktown Heights, N. Y.* (Plenum, New York, 1973), p. 491.

[10]S. T. Picraux, W. L. Brown, and W. M. Gibson, Phys. Rev. B 6, 1382 (1972).

[11]R. B. Alexander, thesis (University of Oxford, 1971; UKAEA Report, 1971) (unpublished).

[12]J. Lindhard, K. Dan. Videnskab. Selskab, Mat.-Fys. Medd. 34, No. 14 (1965).

[13]R. B. Alexander, P. T. Callaghan, and J. M. Poate, in Ref. 9, p. 477.

[14]D. V. Morgan and D. Van Vliet, Rad. Effects 12, 203 (1972).

[15]J. W. Mayer, L. Eriksson, and J. A. Davies, *Ion Implantation in Semiconductors* (Academic, New York, 1970), Chap. 4.

[16]J. B. Marion and F. C. Young, *Nuclear Reaction Analysis* (North-Holland, Amsterdam, 1968).

[17]L. C. Northcliffe and R. F. Schilling, Nuclear Data Tables A 7, 233 (1970).

[18]F. Abel, G. Amsel, M. Bruneaux, C. Cohen, B. Maurel, S. Rigo, and J. Roussel, J. Radioanalytical Chem. (to be published).

[19]W. J. McG. Tegart, The Electrolytic and Chemical Polishing of Metals in Research and Industry, 2nd ed. (Pergamon, London, 1959).

[20]K. C. Knox, Nucl. Instrum. Meth. 81, 202 (1970).

[21]T. M. Buck, J. M. Poate, K. A. Pickar, and C. M. Hsieh, Surf. Sci. 35, 362 (1973).

[22]R. A. Boie and H. P. Lie (unpublished).

[23]K. Björkqvist and B. Domeij, Rad. Effects 13, 191 (1972).

[24]See, for example, J. E. Westmoreland, J. W. Mayer, F. H. Eisen, and B. Welch, Rad. Effects 6, 161 (1970).

[25]R. B. Alexander and P. T. Callaghan, Phys. Lett. 45A, 379 (1973).

[26]This follows from the equivalence of the crystal point group and the group consisting of the inverse operations of the point group.

[27]F. H. Eisen and E. Uggerhøj, Rad. Effects 12, 233 (1972).

[28]J. H. Barrett, Phys. Rev. B 3, 1527 (1971).

[29]H. D. Carstanjen and R. Sizmann, Rad. Effects 12, 225 (1972).

[30]J. U. Andersen, K. Dan. Videnskab. Selskab, Mat.-Fys. Medd. 36, No. 7 (1967).

[31]See, for example, C. Erginsoy, Phys. Rev. Lett. 15, 360 (1965).

[32]L. Meyer, Phys. Status Solidi 44, 253 (1971).

[33]M. T. Robinson, Phys. Rev. B 4, 1461 (1971).

[34]W. M. Gibson and J. Golovchenko, Phys. Rev. Lett. 28, 1301 (1972).

[35]J. U. Andersen and L. C. Feldman, Phys. Rev. B 1, 2063 (1970).

[36]L. Pauling, *The Nature of the Chemical Bond*, 3rd ed. (Cornell U. P. Ithaca, N. Y., 1960).

[37]R. S. Nelson (Harwell; private communication).

[38]J. W. Christian, *The Theory of Transformations in Metals and Alloys* (Pergamon, Oxford, England, 1965), Chap. XVI.

[39]P. A. Thackery and R. S. Nelson, Philos. Mag. 19, 169 (1969).

[40]H. de Waard, in *Mössbauer Spectroscopy and its Applications* (IAEA, Vienna, 1972), p. 123.

[41]H. de Waard (Groningen; private communication).

[42]S. A. Drentje and J. Ekster (National Laboratory Groningen Report, 1969) (unpublished).

[43]P. T. Callaghan, R. B. Alexander, and N. J. Stone (unpublished).

[44]A. T. Hirshfeld, D. D. Hoppes, W. B. Mann, and F. J. Schima, in *Hyperfine Interactions in Excited Nuclei*, edited by G. Goldring and R. Kalish (Gordon and Breach, New York, 1971), Vol. I, p. 335.

[45]*American Institute of Physics Handbook*, 3rd ed., edited by D. E. Gray (McGraw-Hill, New York, 1972), p. 4-115.